Nonlinear Ultrasonic Evaluation of Disorderedly Clustered Pitting Damage Using An *in-situ* Sensor Network

Wuxiong CAO[a,b‡ζ], Kai WANG[b‡], Pengyu ZHOU[bζ], Xiongbin YANG[bζ], Lei XU[bζ], Menglong LIU[c], Paul FROMME[d], Baojun PANG[a], Runqiang CHI[a], and Zhongqing SU[b,e*]

[a] School of Astronautics
Harbin Institute of Technology, Harbin 150080, P.R. China

[b] Department of Mechanical Engineering, The Hong Kong Polytechnic University,
Kowloon, Hong Kong Special Administrative Region

[c] School of Mechanical Engineering and Automation
Harbin Institute of Technology, Shenzhen 518052, P.R. China

[d] Department of Mechanical Engineering
University College London, London, United Kingdom

[e] The Hong Kong Polytechnic University Shenzhen Research Institute,
Shenzhen 518057, P.R. China

Submitted to *Structural Health Monitoring-An International Journal*
(submitted on 25th September 2019; revised and re-submitted on 23rd January 2020)

---

‡ These authors contributed equally to this work.
ζ PhD candidate
* To whom correspondence should be addressed. Tel.: +852-2766-7818, Fax: +852-2365-4703
Email: Zhongqing.Su@polyu.edu.hk (Prof. Zhongqing SU, *Ph.D.*)

Abstract

Pervasive but insidious, pitting damage – from pitting corrosion in maritime structures through electrical pitting in bearings to debris cloud-induced pitting craters in spacecraft, is a typical modality of material degradation and lesion in engineering assets in harsh service environment. Pitting damage may feature hundreds of clustered, localized craters, cracks and diverse microscopic defects (*e.g.*, dislocation, micro-voids and cracks) disorderedly scattered over a wide area. Targeting accurate, holistic evaluation of pitting damage (mainly the existence, location and size of the pitted area), an insight into the generation of nonlinear features in guided ultrasonic waves (*i.e.*, high-order harmonics) that are triggered by pitting damage is achieved using a semi-analytical finite element (SAFE) approach, based on which a monotonic correlation between the nonlinear ultrasonic features and the holistic severity of pitting damage is established. With such correlation, a structural health monitoring framework is developed, in conjunction with the use of an *in-situ* sensor network comprised of miniaturized piezoelectric wafers, to characterize pitting damage accurately and monitor material deterioration progress continuously. The framework is experimentally validated, in which highly complex pitting damage in a space structure, engendered by a hypervelocity debris cloud, is evaluated precisely.

***Keywords*:** structural health monitoring; nonlinear ultrasonic evaluation; pitting damage; contact acoustic nonlinearity; *in-situ* sensor network

1. Introduction

Pitting damage is a prevailing modality of material lesion in engineering assets. Amid numerous examples are pitting corrosion in maritime structures[1-3], electrical pitting in bearings[4,5], pitting craters in orbiting spacecraft induced by space junk or debris clouds[6-8]. Material degradation and deterioration caused by pitting damage, usually initiated at an unperceivable scale but progressing at an alarming speed, can fairly compromise structural reliability, integrity and performance, and without timely awareness lead to fragmentation and even failure of the entire system. This has entailed early detection of pitting damage and accurate assessment of its severity, on which basis follow-up remedial measures can be implemented. However, evaluation of pitting damage is extremely challenging and daunting, because of its highly specific manifestation: in most circumstances a pitting damage area features hundreds of small craters and cracks disorderedly clustered over a wide area ("*pitted region*" hereinafter), with two examples shown in Figure 1.

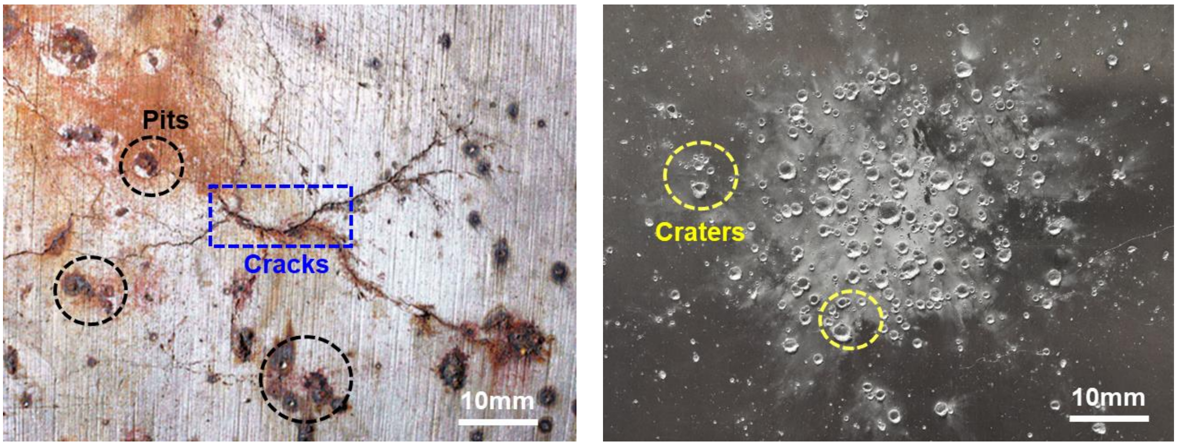

Figure 1. (a) Pitting corrosion in maritime structure[3]; and (b) space debris-cloud-induced pitting craters in a spacecraft structure.

To evaluate pitting damage (or *pitted region*), nondestructive evaluation (NDE) techniques[9-11] can be employed, as typified by radiography, shearography, holography, eddy-current, thermography and resonance imagery. Nevertheless, with a nature of off-line inspection performed at regularly scheduled intervals and a high degree of human interference in result interpretation, most of NDE techniques are inherently unwieldy to early awareness of pitting damage, let alone continuous monitoring of its progress. They are costly, time-consuming, labor-intensive, yet unable to inspect the parts inaccessible to bulky NDE transducers. Moreover, prevailing NDE techniques have demonstrated effectiveness only when a pitted region is macroscopically formed.

In lieu of conventional NDE approaches, guided ultrasonic wave (GUW)-based inspection[12-17] has proven capability of striking a balance among resolution, detectability, practicality, and cost. The premise of GUW-based detection lies in the fact that interaction between GUWs and damage will change wave propagation attributes, inducing delay in arrival time of wave packet, attenuation of wave energy, wave scattering, and mode conversion among others, in which rich information pertaining to damage is encoded. Nonetheless, existing GUW-based approaches[18-29] are demonstrably effective only for singular damage of a regular form (*e.g.*, a crack or a hole), or multiple damages that are sufficiently apart (to avoid mutual interference among waves scattered by multiple damages).

In the attempt to evaluate disorderedly clustered pitting damage that features multitudinous craters and cracks co-existing in a highly localized area, existing GUW-based inspection is confronted with the following challenge:

(i) pitting craters and cracks are densely clustered, and thus the GUWs, which are scattered by the craters or cracks with dimensions comparable to the probing wavelength, are severely tangled and overlapped, presenting high complexity of signal appearance and obfuscation of damage-associated signal features;

(ii) or, if the dimensions of pitting craters and cracks are much less than a probing wavelength, no significant wave scattering as stated in (i) will be induced, and this will result in absence of discernable changes in wave propagation attributes. As a consequence, these undersized craters or cracks may be underestimated or overlooked.

Treating the whole pitted region as singular damage by ignoring individual craters and cracks within the pitted region may avoid the above challenge, however such a compromise restricts the detection at a qualitative or quasi-quantitative level – indicating only the existence and approximate periphery of a pitted region, and failing to describe the severity of a pitted region in a quantitative manner.

To circumvent the above deficiency of conventional GUW-based inspection, nonlinear features of GUWs have been increasingly exploited, in line with the fact that damage introduces a certain degree of nonlinearity to the probing GUWs that can be more sensitive than the linear signal features (*e.g.*, delay in arrival time and attenuation of wave energy) to undersized damage[24-30]. Methods in this category are represented by those using the first-, second-, or sub-harmonics, mixed frequency responses, or shift in resonance frequency[18-22]. Most of these approaches address an abnormal intensification in material nonlinearity due to the existence of damage, along with emergence of damage-induced contact acoustic nonlinearity (CAN)[31-34].

Even though, the evaluation of pitting damage using nonlinear features of GUWs, in a quantitative and precise manner, is hitherto still a highly challenging task, and relevant research is indeed almost absent, let alone to extend off-line detection of pitting damage to the on-line, continuous monitoring of its deterioration. In recognition of this, the energy shift from the fundamental wave modes to high-order harmonic modes when a probing GUW traverses a pitted region is interrogated in this study using a semi-analytical finite element (SAFE) approach, aimed at quantitatively correlating the nonlinear ultrasonic features with the relative severity of pitting damage. Numerical simulation is implemented for proof-of-concept verification. On this basis, a structural health monitoring (SHM) framework is developed, in conjunction with the use of an *in-situ* sensor network comprised of miniaturized piezoelectric wafers, for quantitatively characterizing pitting damage (mainly focusing on the location and size of the pitted area) and continuously monitoring its deterioration. As practical implementation, the framework is used to evaluate pitting damage in a space structure that is generated by a hypervelocity debris cloud.

2. Principle of Approach: Nonlinear Features of GUWs induced by Pitting Damage

When traversing a pitted region, a probing GUW is modulated, diverting partial wave energy from the excitation frequency to integer multiple or fractional multiple of the excitation frequency, namely the generation of high-order harmonics. These harmonics are commonly referred to as super-harmonics and sub-harmonics, respectively[18-22]. In virtue of their sensitivity to microstructural degradation associated with dislocation substructures, second phase precipitates, micro-void/crack nucleation and irradiation[23-25], the high-order harmonics are appealing nonlinear features of GUWs for ultrasonic evaluation.

Featuring a large quantity of clustered, localized, small-scalar craters and cracks with numerous dislocations and sub-grains, a pitted region introduces plastic deformation and consequently plastic strains to polycrystalline solids of the material[35-37]. The interaction of craters and cracks with a probing GUW embraces two alternating phases: (i) crack opening during the tensile stage of GUW propagation, which triggers wave scattering and mode conversion; and (ii) crack closing during the compressional stage, in which wave propagation remains unchanged without distortion. Together, both jointly drive the crack to manifest a "breathing" manner and give rise to the generation of CAN[31-33]. Thus, the severity of pitting damage (represented by the dislocation density) is correlated to the different degrees of collective manifestation of plastic strain in the material, which can be calibrated with the magnitude of the generated second harmonic mode – one of the key nonlinear features of GUWs. Such an interaction between a probing GUW and pitting damage takes place at the microscopic level and the generated nonlinear features, compared with their linear counterparts used in linear ultrasonic techniques (such as delay in time of flight or attenuation of wave magnitude), are more sensitive to minute dislocations and micro-cracks in a pitted region.

To better understand the generation of high-order harmonics and use them for quantitative evaluation of pitting damage, a dedicated modeling approach is developed. Consider an isotropic, homogeneous solid medium which is in its intact state, the nonlinearities in a propagating GUW originate from two major sources (during analytical derivation): the intrinsic material nonlinearity and the geometric (or convective) nonlinearity[35]; when the medium contains inherent imperfections (*e.g.*, lattice abnormality, precipitates and vacancies) or material lesion (*e.g.*, crack), additional nonlinearity will be embodied in the GUW. The intrinsic material nonlinearity refers to the intrinsic nonlinear elasticity of lattices, while the geometric nonlinearity is owing to the mathematic relation between the Eulerian coordinates and Lagrangian (material) coordinates. In the model, the nonlinearity is depicted using a three-dimensional (3-D) stress-strain relation with a second-order approximation[38], as

$$\sigma_{ij} = (C_{ijkl} + 1/2\, M_{ijklmn}\varepsilon_{mn})\varepsilon_{kl}\,, \tag{1}$$

where $C_{ijkl} = \lambda\delta_{ij}\delta_{kl} + 2\mu I_{ijkl}$. σ_{ij} denotes the stress tensor, ε_{mn} and ε_{kl} the strain tensors, and C_{ijkl} the second-order elastic (SOE) tensor defined with Lamé parameter λ and μ. M_{ijklmn} a tensor simultaneously accounting for the above two types of nonlinearities via[39]

$$M_{ijklmn} = C_{ijklmn} + C_{ijln}\delta_{km} + C_{jnkl}\delta_{im} + C_{jlmn}\delta_{ik}, \tag{2}$$

where

$$\begin{aligned} C_{ijklmn} = & \frac{1}{2}\mathcal{A}(\delta_{ik}I_{jlmn} + \delta_{il}I_{jkmn} + \delta_{jk}I_{ilmn} + \delta_{jl}I_{ikmn}) \\ & + 2\mathcal{B}(\delta_{ij}I_{klmn} + \delta_{kl}I_{mnij} + \delta_{mn}I_{ijkl}) + 2\mathcal{C}\delta_{ij}\delta_{kl}\delta_{mn}. \end{aligned} \tag{3}$$

In the above, C_{ijklmn} is the third-order elastic (TOE) tensor describing material nonlinearity, which is directly related to three TOE constants (*i.e.*, $\mathcal{A}$, $\mathcal{B}$ and $\mathcal{C}$). The last three terms of Eq. (2) together address geometric nonlinearity. δ_{ik} and such in similar forms are the Kronecker deltas. I_{jlmn} and such in similar forms are the fourth-order identity tensors. The intrinsic material nonlinearity is related to its SOE and TOE constants, via., $\overline{C}_{1111}$ and $\overline{C}_{111111}$, respectively, which reads[40,41]

$$\beta_{mat} = \frac{8}{k^2 x}\left(\frac{A_2}{A_1^2}\right) = \frac{3\overline{C}_{1111} + \overline{C}_{111111}}{\overline{C}_{1111}} \propto \frac{1}{2}\left(3 + \frac{2\mathcal{A} + 6\mathcal{B} + 2\mathcal{C}}{E}\right). \tag{4}$$

Obviously, the material nonlinearity β_{mat} is governed by Young's modulus E and three TOE constants. As the three TOE constants are correlated to plastic deformation caused by such as fatigue, thermal aging and shock hardening, the nonlinearity parameter is accordingly linked to the plasticity-driven material damage including pitting damage.

Morphological analysis, conducted by the authors in their earlier study[6], reveals that in a typical pitted region, on top of a large quantity of macro-scale craters and cracks, diverse microstructural changes, for instance micro-voids, micro-cracks, recrystallized fine grains and dislocations, co-exist, as observed in the example shown in Figure 2. These recrystallized fine grains, dislocation substructures and shock hardening jointly lead to an increase in material plasticity and hence intensification in material nonlinearity[35,36,42,43]. In general, such intensification in material nonlinearity incurred by the pitting damage imposes remarkable influence on probing wave propagation more than the intrinsic material nonlinearity does. In the analytical model, the localized intensification in the material nonlinearity in the pitted region is depicted using the increasing in the three TOE constants (*i.e.*, $\alpha\mathcal{A}$, $\alpha\mathcal{B}$ and $\alpha\mathcal{C}$, α is the scale factor)[43,45]. In addition, numerous micro-voids expand to form micro-cracks and then macroscopic cracks, as illuminated in Figure 3, interaction of a probing GUW with which gives rise to the generation of CAN.

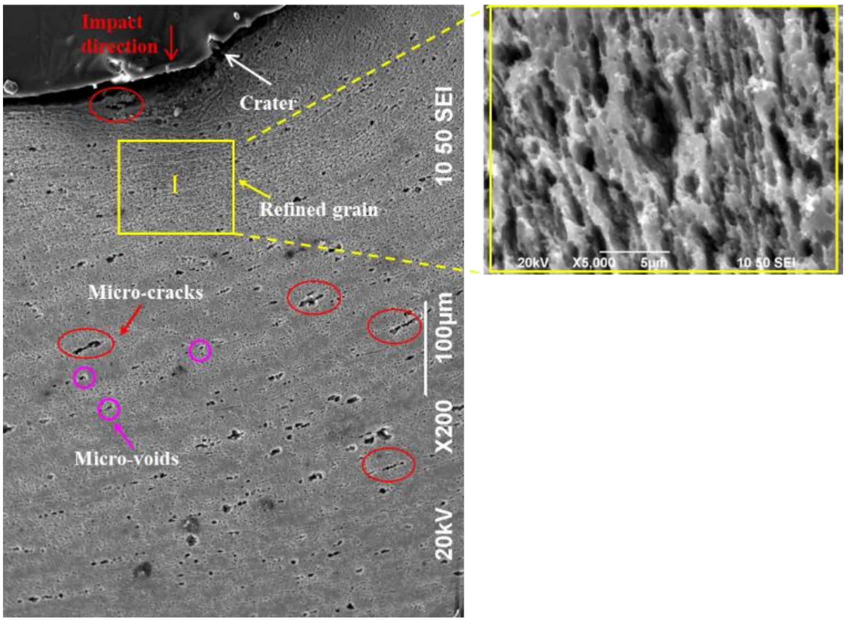

Figure 2. Scanning electron microscope (SEM, JEOL JSM-6490) image of material microstructure underneath a pitted region produced by a hypervelocity debris cloud[6].

In a similar vein, using the pitting corrosion that is ubiquitous in maritime structures as another example, in addition to the corrosion pits and cracks at the surface layer, stress-corrosion cracking (SCC) initiates at these pits and micro-cracks, as shown schematically in Figure 4(a). The SCC-induced cracks propagate along the grain boundaries under external stress[44,45] that are referred to as inter-granular SCC (IGSCC), in Figures 4 (b) and (c). In general, these micro-cracks can distort and modulate the propagation of probing GUWs and trigger CAN.

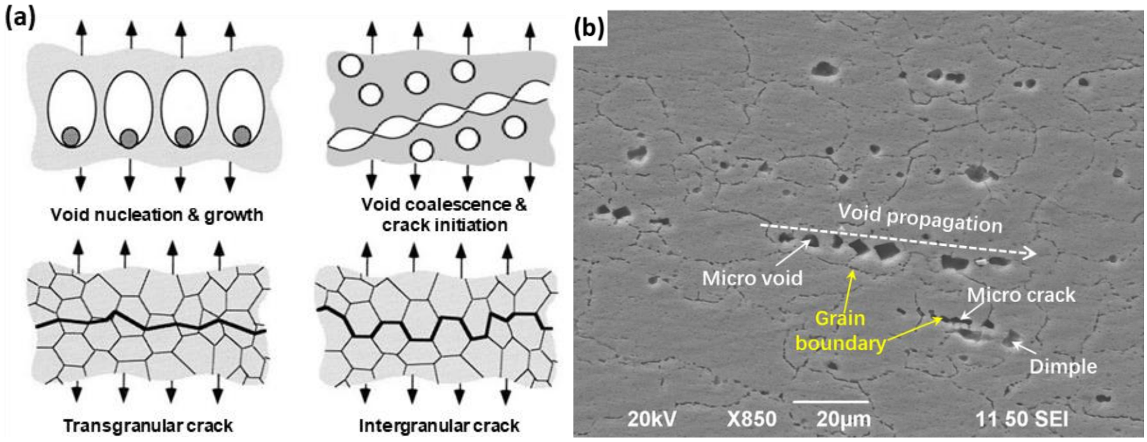

Figure 3. (a) Schematic of void nucleation, growth and coalescence under hypervelocity debris cloud impact process; and (b) SEM image of material microstructure underneath a pitted region, showing void nucleation and propagation.

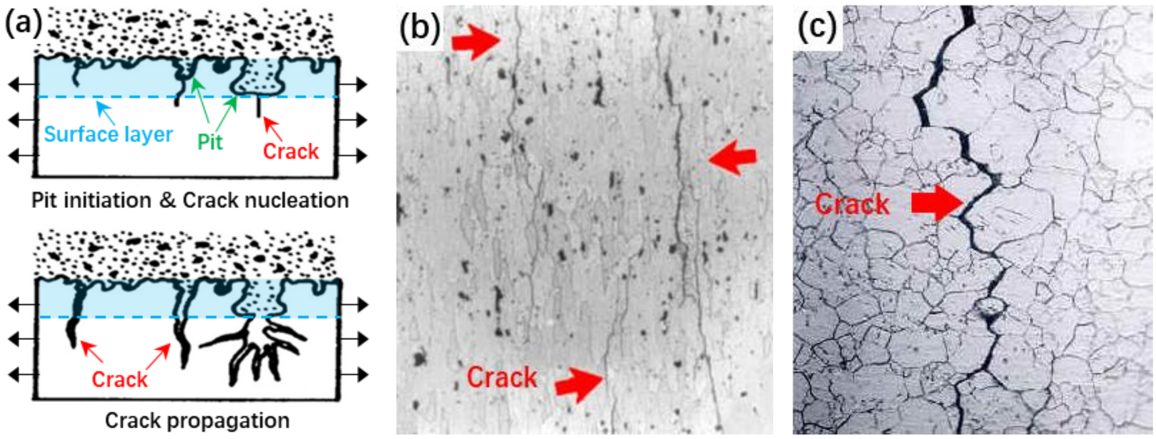

Figure 4. (a) Schematic view of SCC propagation; (b) IGSCC in 7075-T6 alloy (picture width: 500 μm)[44]; and (c) IGSCC in aluminum alloy tube (Mag: 500X)[45].

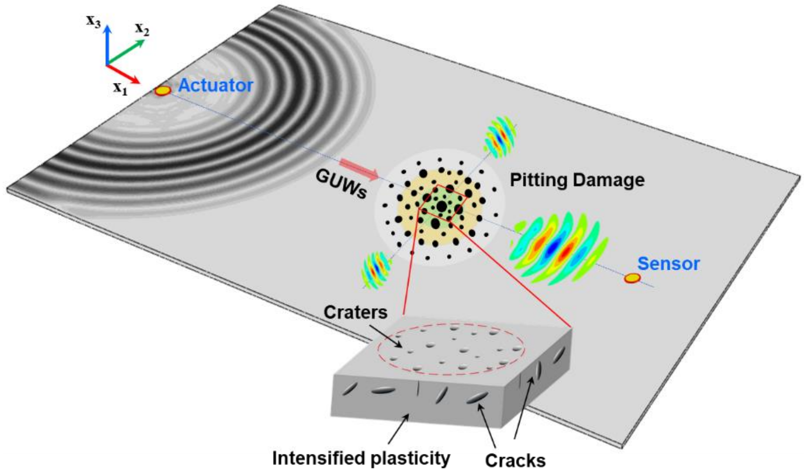

Figure 5. A plate-like waveguide bearing a pitted region (containing intensified plasticity, craters and "breathing" cracks).

A plate-like waveguide containing a pitted region is illustrated schematically in Figure 5. The "breathing" behavior of micro-cracks introduce nonlinearities to scattered waves, serving as a secondary wave source located at the micro-crack – called "*crack-induced secondary source*" (*CISS* hereinafter) in the model, as detailed in the authors' earlier works[32,33]. *CISS* features time-dependent traits and initiate high-order harmonics. The in-plane displacement ($U_n^{S-2f_0}$) of *CISS*-induced n^{th}-order symmetric modes at the double excitation frequency ($2f_0$) can be ascertained as[32,33]

$$U_n^{S-2f_0} = A_n^S u_n^S(x_3)\left[H_0^2(k_n r) - \frac{1}{k_n r}H_1^2(k_n r)\right], \tag{5}$$

where

$$A_n^S = \frac{k_n}{4i}\frac{2CISS_{in}^{bre-2f_0}\cdot u_n^S(0)}{I_{nn}^S}.$$

In the above, f_0 signifies the angular frequency of the probing GUW excited at fundamental frequency f_0, $U_n^{S-2f_0}$ the *CISS*-induced in-plane displacement at $2f_0$ (superscript S denoting the symmetric mode, and subscript n representing the n^{th} order), $u_n^S(x_3)$ the in-plane displacement of wave mode as a function of x_3 (see Figure 5), κ_n the wave number of the propagating wave mode at $2f_0$, $H^2(\square)$ the Hankel function of the second kind, and r the distance from the crack to the sensor at which GUW is captured. A_n^S is the crack-induced wave fields at $2f_0$, i the imaginary unit, I_{nn}^S the energy carried by the Lamb wave mode, and $u_n^S(0)$ the in-plane displacement of wave mode at the middle of the plate. $CISS_{in}^{bre-2f_0}$ is the in-plane component of $\overrightarrow{CISS}^{bre-2f_0}$ (the modulated *CISS* attributed to the "breathing" behavior at $2f_0$).

It can be seen that the generation of the second harmonic of the probing GUW can be attributed to $\overrightarrow{CISS}^{bre-2f_0}$. With the CAN induced by the "breathing" behavior of micro-cracks in the pitted region, the second harmonic in GUW signals will be intensified. The modeling of nonlinearities (*i.e.,* high-order harmonics) generation upon interaction of a probing GUW with pitting damage provide a theoretical basis for quantitative characterization of pitting damage in this study.

3. Damage Index Definition Using Semi-Analytical Finite Element (SAFE) Approach

Based on the above modeling of nonlinearity introduced by pitting damage, a *nonlinear index* (*NI*) is proposed to quantify the degree of nonlinearity against degree of pitting damage. Using a SAFE approach, the index is defined as

$$NI = \frac{U_n^{S-2f_0}}{(U_n^{S-f_0})^2}, \tag{6}$$

where $U_n^{S-f_0}$ signifies the magnitude of the probing GUW excited at f_0, and $U_n^{S-2f_0}$ the magnitude of pitting damage-induced nonlinearity at double excitation frequency ($2f_0$).

Finite element simulation is performed using ABAQUS®/EXPLICIT, in which the analytical solutions obtained in preceding section are recalled in a user-defined subroutine (VUMAT) – a SAFE approach. A two-dimensional (2-D) finite element model for an aluminum plate (1000 mm long), containing a pitted region of a diameter of 50 mm, is developed, as displayed in Figure 6, and the model is discretized with the four-node plane strain (CPE4R) elements. In the pitted region, nine craters with a diameter of 1 mm for each are uniformly distributed at the surface of the pitted region at an interval of 4 mm.

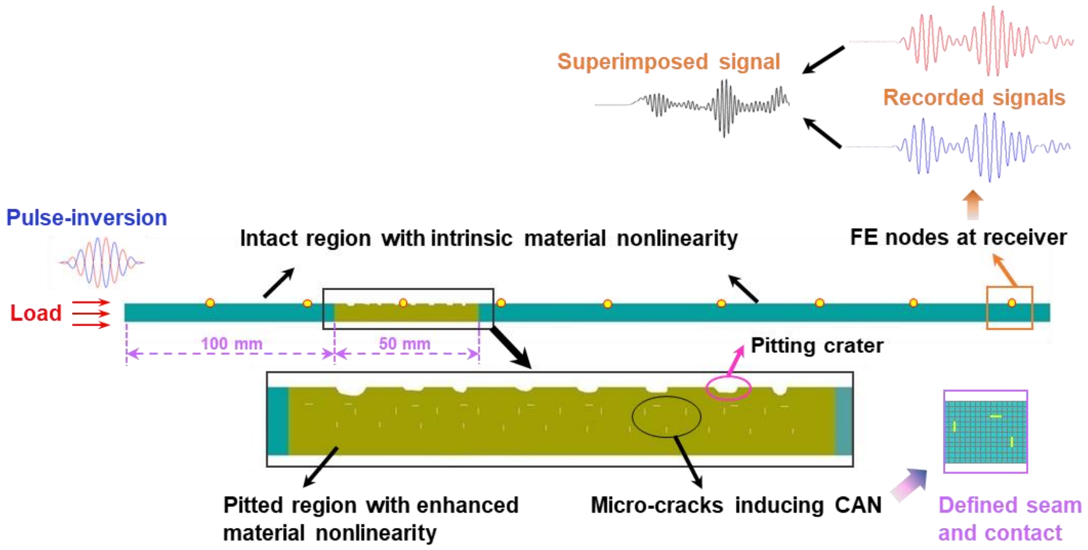

Figure 6. 2-D FE model of the plate-like waveguide bearing the pitted region.

As discussed in Section 2, possible sources of nonlinearity in the waveguide include the plasticity-induced nonlinearity and the CAN on top of intrinsic material nonlinearity, all of which are taken into account in the model. To model the intensified material nonlinearity in the pitted region, the TOE constants increase equally up to $\alpha\mathcal{A}$, $\alpha\mathcal{B}$ and $\alpha\mathcal{C}$ for this region, where the scale factor α is assumed to be 1.5 (compared with 1.0 for an intact waveguide) according to large volume compression of the material (35~50%) that is caused by debris cloud impact[6], as listed in Table 1. Note that the TOE constants are negative, reflecting the trend of elastic stiffness of materials against the variation of interatomic distance induced by material status changes. Modeling of intrinsic and intensified material nonlinearities is implemented in VUMAT using the nonlinear stress-strain relation. To model the micro-cracks beneath the craters in the pitted region, N ($N=28$ for the 3 mm thick plate, $N=47$ for the 5 mm thick plate) seam cracks with a length of a ($a=0.2\,\mathrm{mm}$) for each are defined and distributed uniformly with an area S , as seen in Figure 6. To be consistent with experimental configuration in the following, nine seam cracks in parallel with the waveguide surface are defined beneath the nine craters, along with other cracks along the thickness direction. Note that the number of cracks beneath the craters can be different under different impact conditions. A contact-pair interaction definition, which prohibits the penetration of nodes into opposite surface is imposed on the two contacting interfaces for each micro-crack for describing the “breathing” behavior when probing GUWs traverse. The crack density V_{crack} is calculated to be 0.0075 using a dimensionless parameter $V_{crack} = Na^2 / S$.

Table 1. Material parameters of the plate-like waveguide in simulation

Aluminum plate	Three TOE constants			Elastic modulus (GPa)	Poisson’s ratio	Density (kg/m^3)
	αA (GPa)	αB (GPa)	αC (GPa)			
Intact region (α=1)	-320	-200	-190	68.9	0.3	2660
Pitted region (α=1.5)	-480	-300	-285			

In simulation, two mode pairs, viz., S_0-S_0 at a lower frequency range (0.9 and 1.8 MHz·mm for two S_0 modes) and S_1-S_2 at a higher frequency range (3.59 MHz·mm for S_1 and 7.18 MHz·mm for S_2), are respectively used for different thicknesses of the waveguide, as displayed in Figure 7. To excite an appropriate probing waves, the in-plane displacement of the same amplitude (1×10^{-4} mm) in parallel with the waveguide surface is applied to the left edge of the plate, and under this condition only the symmetric Lamb wave modes are generated. (i) For a plate of 3 mm in its thickness, an eight-cycle Hanning windowed sinusoid tone-burst at a central frequency of 300 kHz is applied to generate the S_0-S_0 mode pair, and under such a loading condition, the fundamental S_0 mode dominates the wave energy. To warrant simulation accuracy, a fine mesh with an element size of 0.1 mm only (*i.e.*, 1/30 of the wavelength of the accordingly generated second harmonic S_0 mode) is applied in the model; (ii) for a plate of 5 mm in thickness, a ten-cycle Hanning-windowed sinusoidal tone-burst at a central frequency of 718 kHz is applied to generate the S_1-S_2 mode pair. Under this loading condition, both the fundamental S_0 mode and S_1 mode are excited. Considering that the sensing points are sufficiently apart from the exciting source, S_1 mode acquired at the sensing points are fairly separated from S_0 modes, because the group velocity of the mode S_1 is much greater than that of S_0 mode at this frequency. This guarantees that S_1 mode can be purely extracted, warranting the accuracy of the obtained amplitudes of S_1-S_2 mode pair. In this case, each element is 0.05 mm in size – 1/50 of the wavelength of the accordingly generated second harmonic S_2 mode. GUW propagation in the waveguide is continuously monitored by measuring the in-plane displacements of the plate surface every 20 mm, Figure 6. Note that the dimension of the plate (*i.e.* 1000 mm) ensures that wave reflections from the right edge of the plate do not interfere with the wave modes of interest.

The in-plane displacements of both the 0° phase and 180° out-of-phase inverted GUWs are extracted at the measurement points and processed with an pulse-inversion approach, with which the weak nonlinearity (*i.e.*, $U_n^{S-2f_0}$ in Eq. (6)) stands out in the superimposed signals and in spectra (obtained via the short-time Fourier Transform (STFT)).

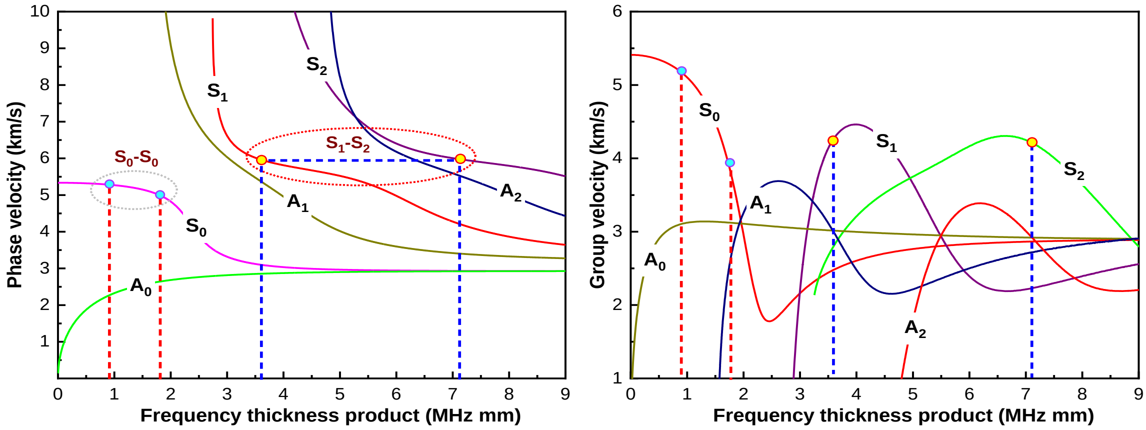

(a) (b)

Figure 7. Dispersion curves for Lamb waves in aluminium alloy plate: (a) phase velocity; and (b) group velocity.

By way of illustration, the simulation results obtained from an intact plate 3 mm thick with pitting damage of different degrees are compared in Figure 8. As observed, with the use of the pulse-inversion approach, the spectral energy of the fundamental S_0 mode (denoted by $S_0^{f_0}$) is remarkably mitigated, while the energy of the second harmonic S_0 mode (denoted by $S_0^{2f_0}$) enhanced. In addition, the energy of sub-harmonic wave ($f_0/2$) is also enhanced.

It can be observed that in the intact plate, the second harmonic modes are generated owning to the intrinsic material nonlinearity (represented by the TOE constants). Compared with the results from the intact plate, the spectral energy at $S_0^{2f_0}$ in the plate with pitting damage is increased phenomenally. It is noteworthy that among various sources of nonlinearity, the intensification of material nonlinearity due to plasticity-driven damage is much weaker than that arising from "breathing" cracks-induced CAN. Together, both of the intensified material plasticity and "breathing" cracks jointly give rise to the accumulation of second harmonics in the waveguide bearing pitting damage.

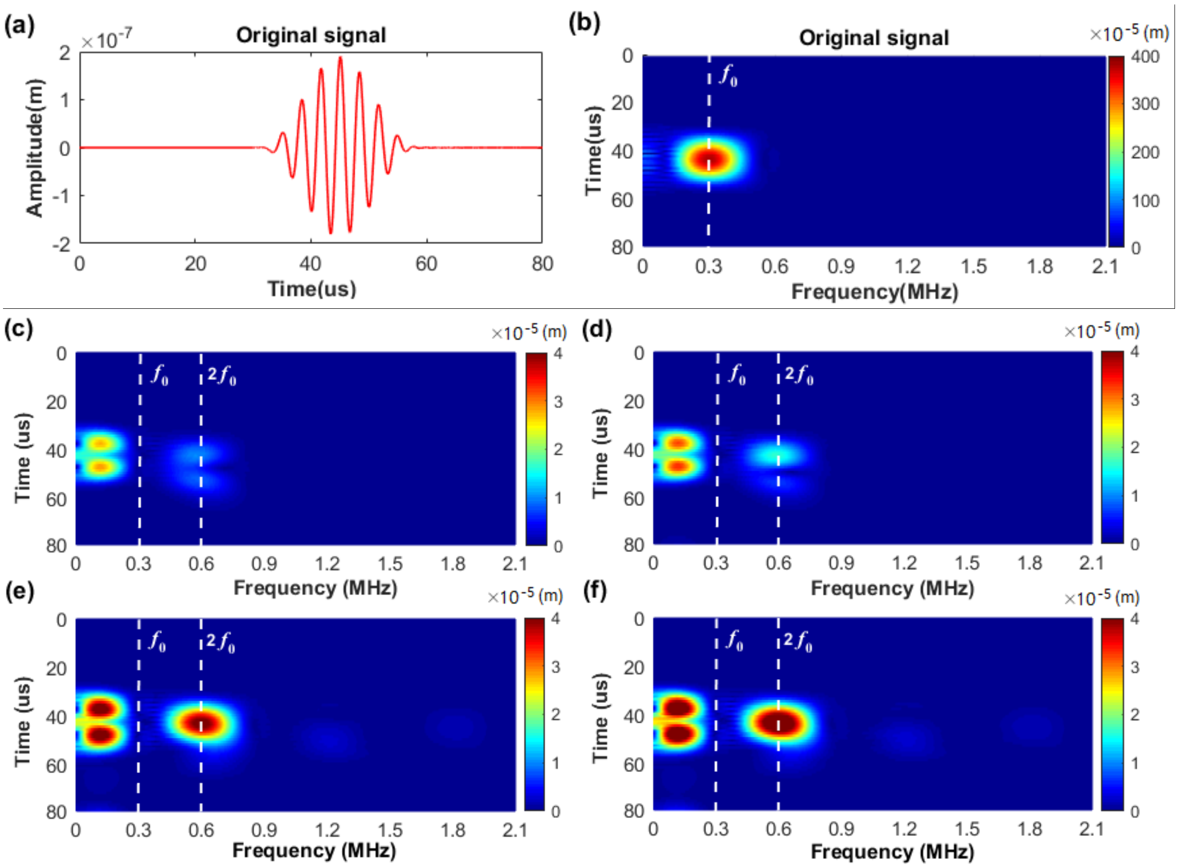

Figure 8. Signals captured at the measurement point 160 mm from the left boundary of the plate (3 mm thick): (a) original signal obtained from the intact plate; (b) spectra of original signal; spectra of superimposed signals acquired via (c) intact plate; (d) pitted plate with enhanced plasticity; (e) pitted plate with seam cracks; and (f) pitted plate with both enhanced plasticity and seam cracks.

To take a step further, *NI* is calculated using Eq. (6) against the propagation distance and different degrees of pitting damage with the mode pair S_0-S_0 or S_1-S_2, and the results are presented in Figure 9. As observed, *NI*, which is obtained when S_0-S_0 mode pair is used, oscillates as the increase of GUW propagation distance – a phenomenon that can be attributed to the inaccurate matching in the respective phase and group velocities of two modes[46] (as seen in Figure 7); while *NI* shows a monotonic and linear increase over the propagation distance when S_1-S_2 pair is used, in which the two modes have the identical phase velocities, exactly satisfying internal resonance conditions. Regardless of the selected mode pairs, the *NI* obtained in the pitted plate (with intensified material plasticity, and "breathing" cracks-induced CAN) is observed to increase significantly after the probing GUWs traverse the pitted region. This phenomenon is remarkable particularly when the probing GUW does not satisfy the requirement of internal resonance (*i.e.*, the phase-velocity matching, and the non-zero power flux) [47], as displayed in Figure 9(a). Thus, both the S_0-S_0 and S_1-S_2 pairs can be used to stand out the damage-induced CAN with comparable effectiveness. It is noteworthy that the plasticity-induced increase in the second harmonic generation delays the decrease in the amplitude of second harmonic modes, which can be attributed to the mismatching of the phase and group velocities, as shown in Figure 9(a).

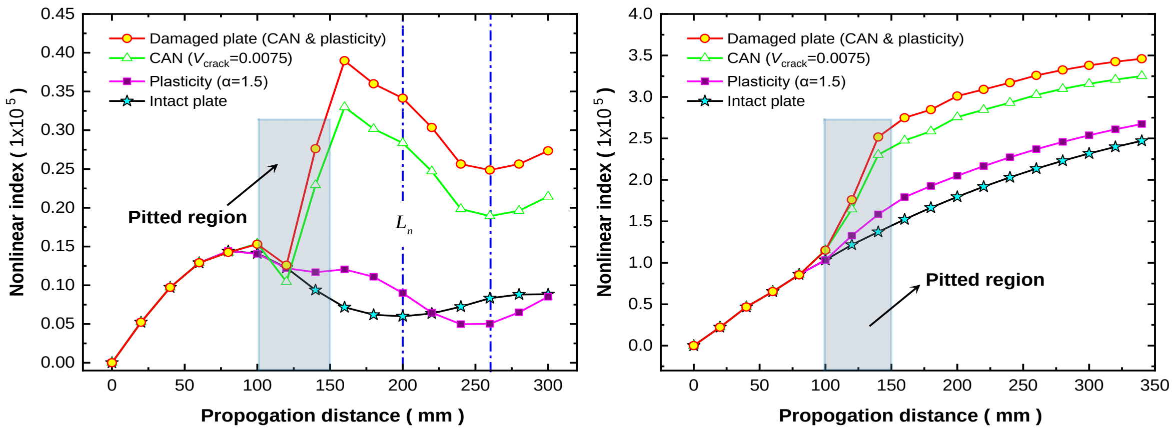

(a) (b)

Figure 9. (a) *NI* obtained in simulation for mode pair S_0-S_0; and (b) *NI* obtained in simulation for mode pair S_1-S_2.

The SAFE results have accentuated the significant influence of the pitting damage on the generation of nonlinearity of GUWs, and inversely the abnormal increase in the nonlinearity of GUWs can be used for characterizing the pitting damage, as demonstrated by the proof-of-concept application in the subsequent session.

4. Proof-of-Concept Application: Characterizing Pitting Damage

The proposed nonlinear ultrasonic evaluation approach is experimentally validated by quantitatively characterizing pitting damage of different modalities.

4.1. Sample Preparation: Creation of Pitting Damage

To create pitting damage in a plate-like waveguide for experimental validation of the proposed evaluation approach, a series of hypervelocity impact (HVI) tests is conducted. A non-powder two-stage light gas gun is used to launch and accelerate a spherical aluminum projectile (AL-2017, Ø 4.5 mm), to impact a typical dual-layered Whipple shield. The Whipple shield consists of a bumper layer (6061-T1, 1 mm in thickness, 300 mm × 300 mm in other two dimensions) and a rear wall layer, Figure 10(a). HVI tests are performed in two scenarios: the projectile impinges the Whipple shield perpendicularly (*normal impact*) and obliquely with an incident angle of 32° (*oblique impact*), respectively, as illustrated schematically in Figure 10(a). The velocity of the projectile is 5.931 km/s in the normal impact and 4.021 km/s in the oblique impact. In both cases, the projectile is sufficient to penetrate the bumper layer. Upon penetration, a debris cloud is created and formed by shattered materials of the bumper layer and projectile, which further impacts the rear wall layer to create multitudinous pitting craters and cracks that are disorderedly scattered in the rear wall layer.

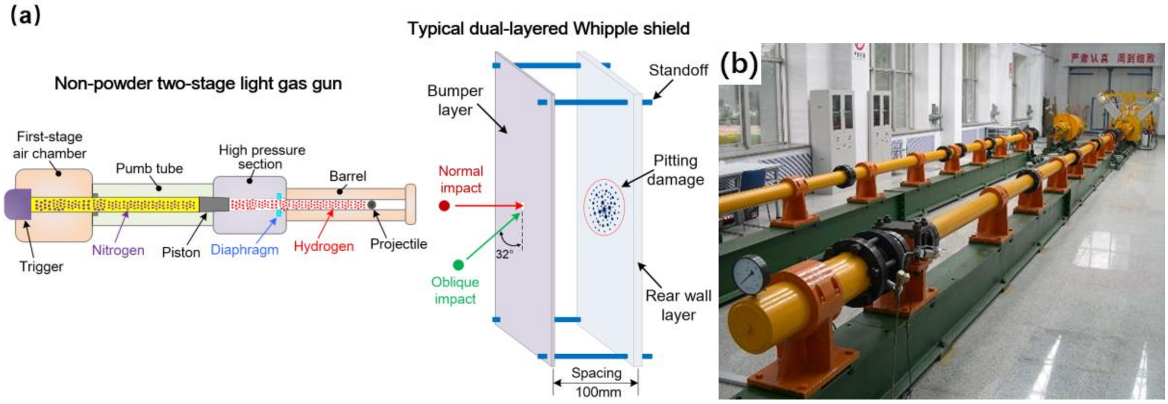

Figure 10. (a) Schematic of HVI test set-up (showing the normal and oblique impact scenarios); and (b) the two-stage light gas gun used for HVI tests.

In the normal impact, a debris cloud that is symmetrical with regard to the *x*-axis impinges the rear wall layer (2024-T4, 3 mm in thickness, 300 mm × 300 mm in dimension). As rigorously investigated in the authors' earlier work[6], the generated cloud feature three key parts: *inner circle debris*, *outer ring debris* and *external bubble debris*, which accordingly creates three pitted areas: *central cratered area* D_{cc}, *ring cratered area* D_{rc}, and *spray area* D_{99}, respectively, as defined in Figure 11(a), all together covering 99% of the scattered pitting craters. Multitudinous pitting craters are mutually nested and overlapped in D_{cc}, while D_{rc} and D_{99} are filled with separated small craters (~100 μm~2 mm in diameter), as photographed in Figure 11(b).

In the oblique impact, a debris cloud, expanding along both the impact direction and the normal direction of the bumper layer, is generated, forming an in-line cloud and a normal debris cloud, respectively, as illustrated schematically in Figure 12(a). These debris clouds subsequently impact the rear wall layer (2024-T4, 5 mm in thickness, 500 mm × 500 mm in dimension), resulting in two separated pitted areas, *i.e.*, A_{d1} and A_{d2}, in which numerous craters with diameters greater than 1 mm are obvious, Figure 12(b).

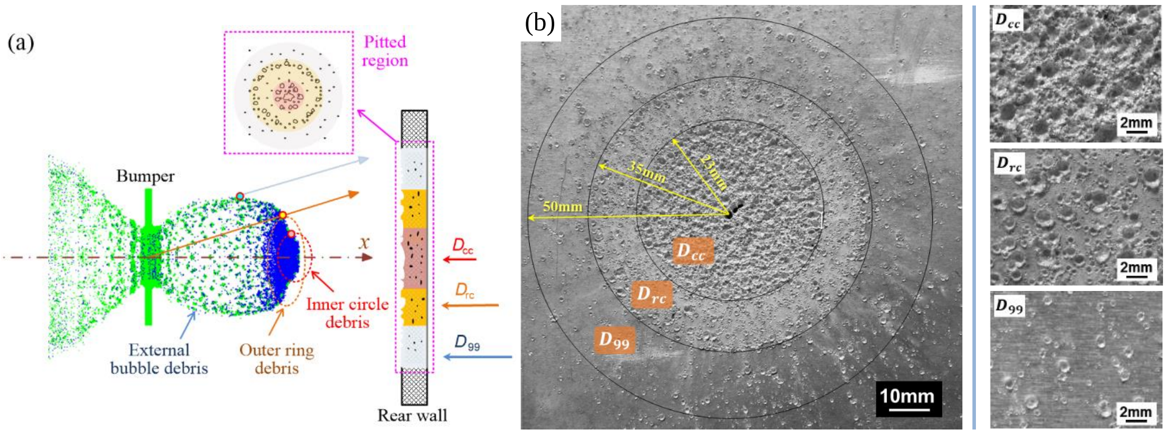

Figure 11. Normal HVI scenario (projectile speed: 5.931 km/s): (a) schematic of debris cloud; and (b) morphology of the debris cloud-produced pitted region.

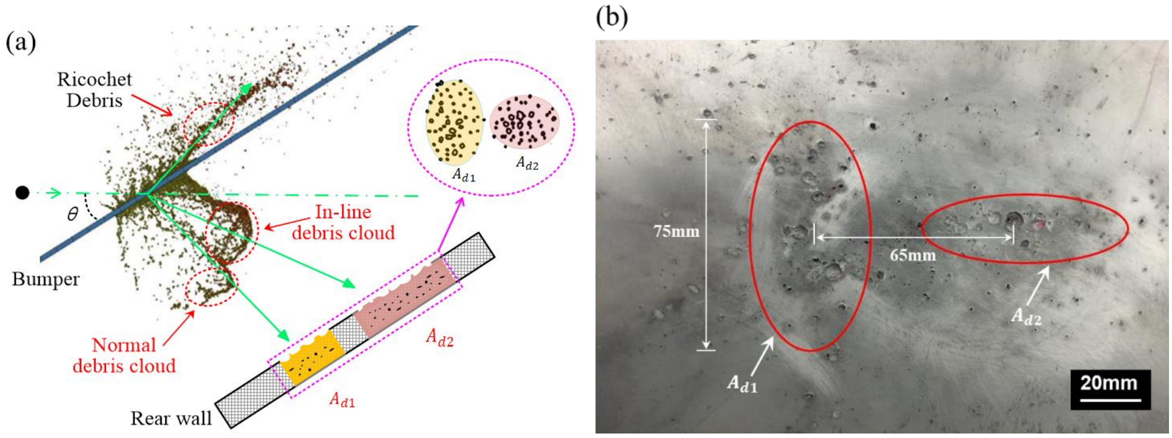

Figure 12. Oblique HVI scenario (projectile speed: 4.021 km/s, incident angle: $\theta = 32^{\circ}$): (a) schematic of debris cloud; and (b) morphology of the in-line debris cloud- and normal debris cloud-produced pitted regions.

4.2. Experiment Set-up

Figure 13 presents the schematic and photograph of the experimental set-up. In the tests, a Hanning-windowed sinusoidal tone-burst signal is generated by a high-power gated ultrasonic system (RITEC® RAM-5000 SNAP). The response voltage signals are acquired by an oscilloscope (Agilent DSO 9064A) and averaged 256 times to minimize measurement uncertainty. A built-in circular sensing network, comprising of 16 miniaturized, lightweight PZT wafers (PSN33, Φ5 mm, thickness: 0.48 mm, denoted by Sen_i ($i = 1, 2, \ldots, 16$)), is mounted on the surface of the rear wall layer. Each of the wafer in the network is alternatively used as actuator and sensor, rendering up to 120 sensing paths, with most paths traversing the pitted regions, as displayed in Figure 13(a). Both the mode pairs S_0-S_0 (0.9-1.8 MHz mm) and S_1-S_2 (3.59-7.18 MHz mm) as investigated in preceding SAFE-based analysis are generated via the system.

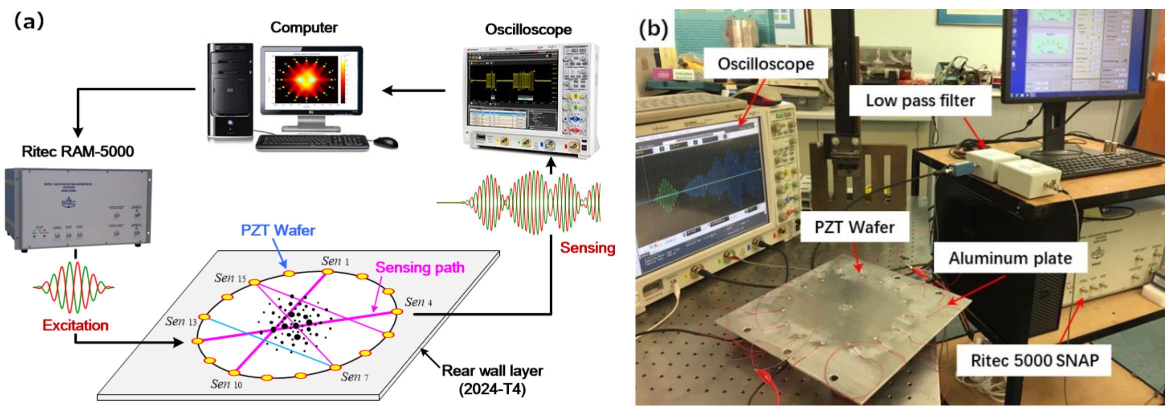

Figure 13. (a) Schematic of experimental set-up for characterization of pitting damage; and (b) photographic illustration of the experiment.

4.3. Signal Processing and *NI* Calculation

In the normal impact scenario, the sensor network covers an inspection region with a diameter of 280 mm, as displayed in Figure 14(a). A seven-cycle Hanning-windowed sinusoidal tone burst at a central frequency of 300 kHz is applied to exploit mode pair S_0-S_0 (0.9-1.8 MHz mm).

The severity degrees of pitting damage in D_{cc}, D_{rc} or D_{99} are usually different significantly, leading to distinct amounts of energy shifted from the fundamental to the second harmonic modes via different sensing paths. By way of illustration, three representative sensing paths (*i.e.*, Sen_1-Sen_9, Sen_1-Sen_8 and Sen_1-Sen_6) with different severity of pitting damage, are selected and accumulation of $S_0^{2f_0}$ mode along these three paths are scrutinized. Figure 14(b) displays both the 0° phase and 180° out-of-phase inverted GUW signals captured via the sensing path Sen_1-Sen_9 that traverses the pitted region center, these two signals are then superimposed to extract the second harmonic mode. The spectra of the original signals and the extracted second harmonic signals obtained via two representative sensing paths (Sen_1-Sen_6 and Sen_1-Sen_9), when the path is intact and contains pitting damage, respectively, are displayed in Figures 14(c) and (d), respectively.

Note that the probing S_0 mode arrives at the sensing point first, and thus it can be easily isolated from other wave modes. Such a trait facilitates accurate extraction of the fundamental and second harmonic modes. It is also noteworthy that the variation in traveling distance of different sensing paths can lead to discrepancy in the amplitudes of second harmonic modes induced by the intrinsic material nonlinearity. However, the damage-induced second harmonic generation is dominant over the traveling distance variation-induced changes in the amplitudes. It can be observed that the incident energy of probing GUW shifts from the fundamental mode to the second harmonic mode, from which the magnitudes of $S_0^{f_0}$ and $S_0^{2f_0}$ modes can be ascertained, shown in Figures 14(e) and (f), on which basis *NI* can be calculated according to Eq. (6) for each sensing path. Note that the defects in the pitted region investigated in this study are of small size, and thus the effect from wave scattering and mode conversion induced by these defects on the defined *NI* is negligible. As observed, the magnitude of $S_0^{2f_0}$ mode increases with the intensification of pitting damage, leading to a higher *NI*, which is consistent with the theoretical and SAFE analysis. Inversely, it is feasible to characterize the pitting damage quantitatively by fusing *NI*s from all the sensing paths in the sensor network.

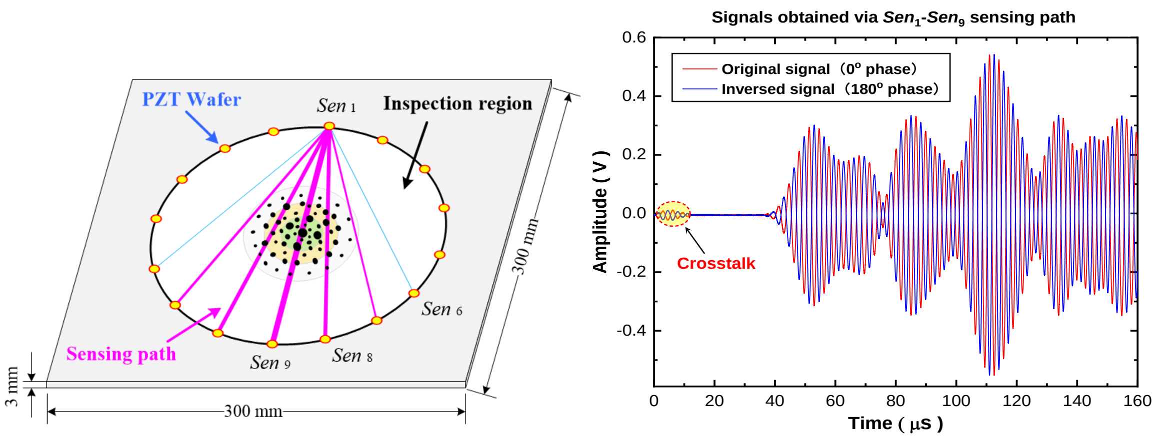

(a) (b)

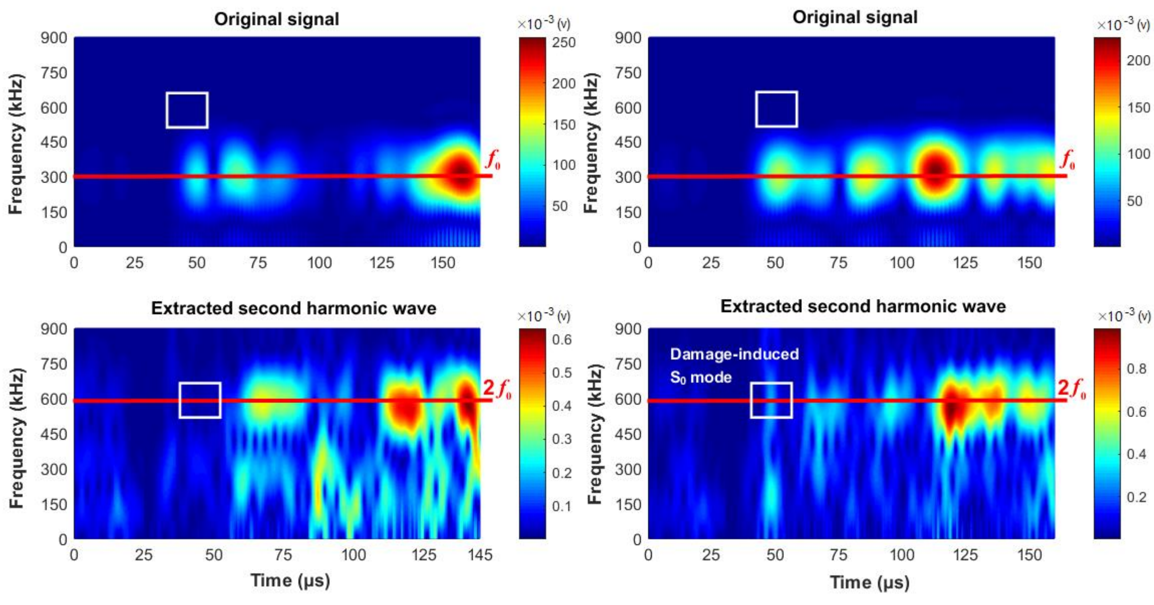

(c) (d)

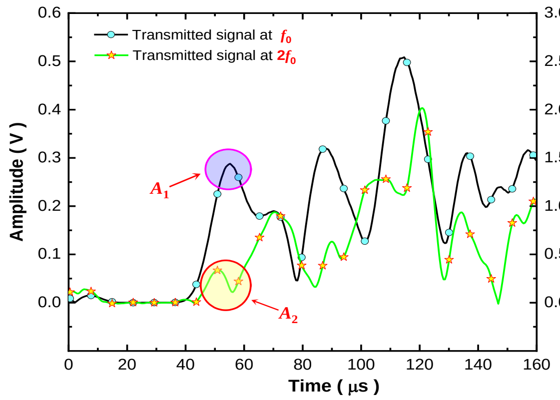

(e)

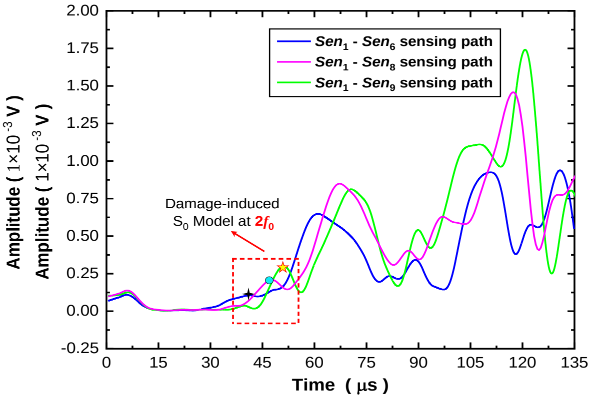

(f)

Figure 14. Normal HVI scenario: (a) schematic of PZT network for characterizing pitting damage; (b) signal acquired via *Sen*$_1$-*Sen*$_9$; (c) and (d) time-frequency spectra of signals acquired via *Sen*$_1$-*Sen*$_6$ and *Sen*$_1$-*Sen*$_9$, respectively; (e) magnitudes of $S_0^{f_0}$ and $S_0^{2f_0}$ modes; and (f) magnitudes of $S_0^{2f_0}$ mode for three representative sensing paths.

As displayed in Figure 15, the severity of pitting damage obtained from all sensing paths is characterized using the defined *NI*. All *NI*s used in the experimental investigations are obtained in the current status, and it does not entail a benchmark process against any baseline signal from the intact plate under certain conditions, offering a baseline-free mechanism to characterize pitting damage. In addition, with the sensor network, 120 sensing paths covering the inspected region are constructed, and the results from all the sensing paths are utilized to image the damage. Considering that the damage of interest is of small scale, there are always paths traversing intact regions. With the approach, the damage manifests itself at pixels featuring high field values, without a need of *a priori* knowledge on the location of pitting damage or a need of making reference to information from sensing paths that traverse the intact region.

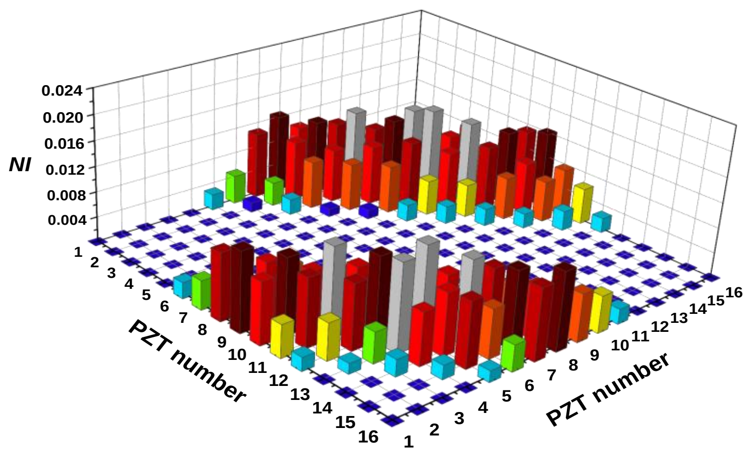

Figure 15. *NI* histogram of pitting damage induced by normal HVI.

Considering morphological shape of the pitted area in the oblique impact scenario, as observed in Figure 12(b), an inspection region with a diameter of 320 mm, greater than that in the normal impact case, is formed by sensor network. Similarly, a ten-cycle Hanning-windowed sinusoidal tone-burst at a central frequency of 718 kHz is applied to exploit mode pair S_1-S_2 (3.59-7.18 MHz mm). Figure 16(b) displays a typical waveform for S_1-S_2 mode pair captured via the sensing path Sen_5-Sen_{13}. Taking the signal acquired via three sensing paths (*i.e.*, Sen_1-Sen_9, Sen_1-Sen_8 and Sen_5-Sen_{13}, as interpreted in Figure 16(a)) as examples, STFT analysis is performed to extract the second harmonic S_2 modes. The spectra of the original signals and the extracted second harmonic signals, obtained via two representative sensing paths (Sen_1-Sen_9 and Sen_5-Sen_{13}), are displayed in Figures 16(c) and (d). These two sensing paths traverse the intact region and damaged region, respectively. Note that the probing S_1 mode arrives at the sensing point first, and thus it can be isolated from other wave modes. This facilitates the accurate extraction of the fundamental and second harmonic modes. It can be observed that the incident energy of probing GUW shifts from the fundamental S_1 mode to the second harmonic S_2 mode, from which the magnitudes of second harmonic modes can be ascertained, shown in Figure 16(e). The magnitude of the second harmonic S_2 mode obtained via the sensing path *Sen*$_5$-*Sen*$_{13}$ is greatest as this sensing path traverses both A_{d1} and A_{d2}, while the one from path *Sen*$_1$-*Sen*$_9$ manifests the lowest value because this sensing path does not cross any pitting damage area. The severity of pitting damage is quantitatively characterized by the *NI*, as demonstrated in Figure 16 (f).

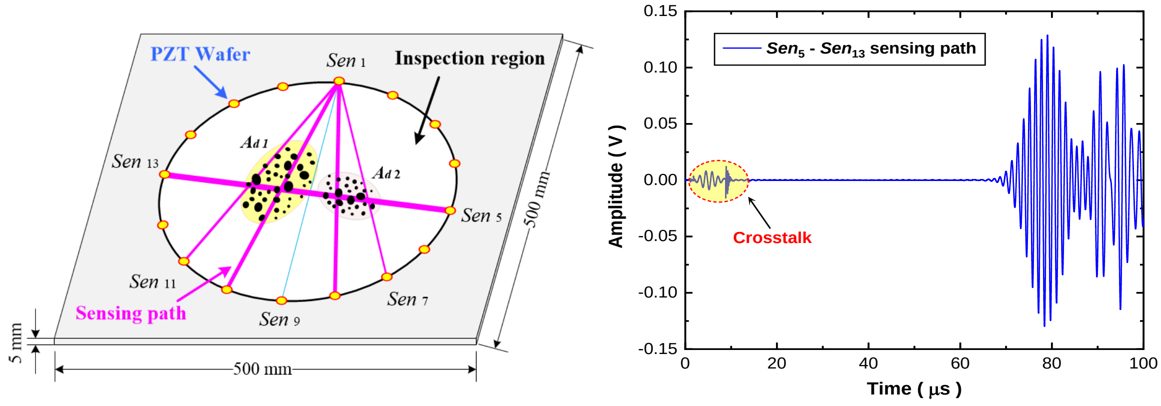

(a) (b)

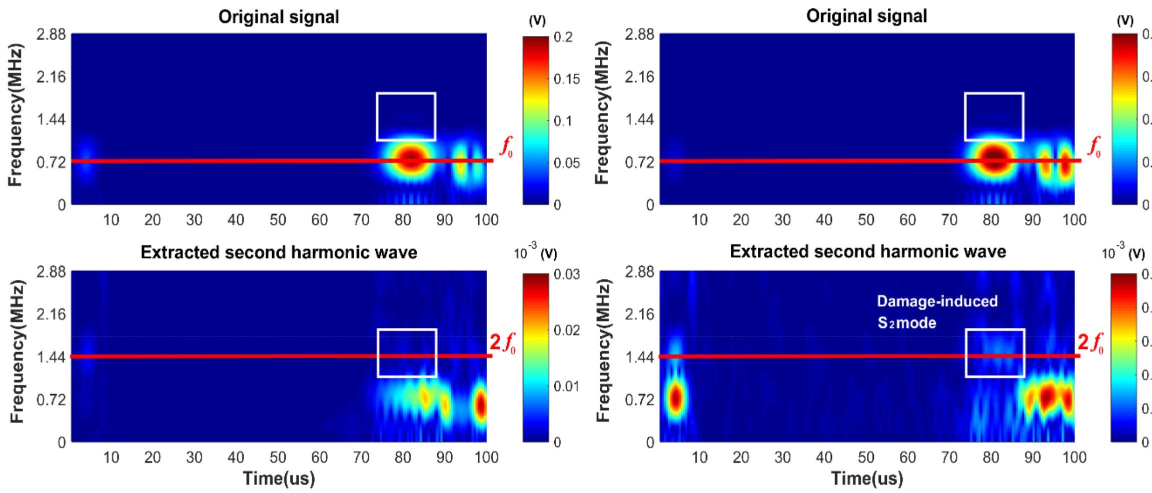

(c) (d)

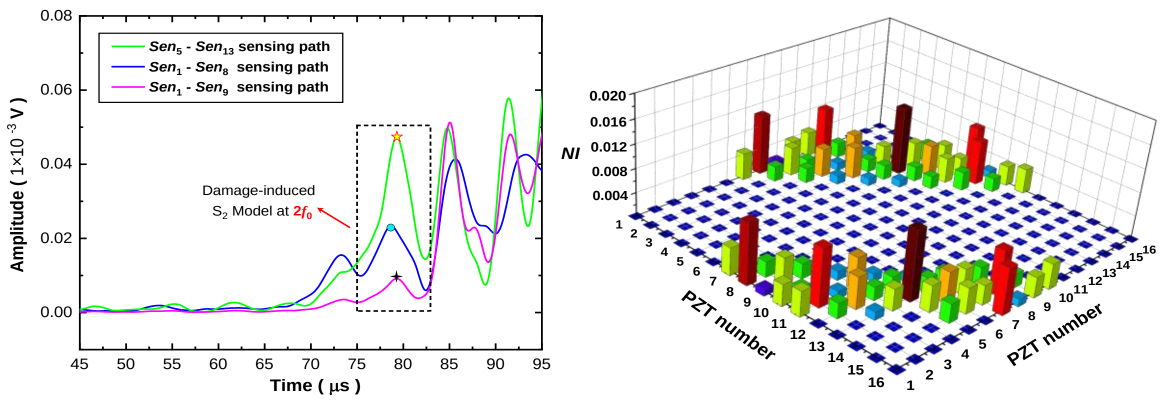

(e) (f)

Figure 16. Oblique HVI scenario: (a) schematic of PZT network for characterizing pitting damage; (b) signal acquired via *Sen*$_5$-*Sen*$_{13}$; (c) and (d) time-frequency spectra of signals acquired via *Sen*$_1$-*Sen*$_9$ and *Sen*$_5$-*Sen*$_{13}$, respectively; (e) magnitudes of S_2 mode for three representative sensing paths; and (f) *NI* histogram of pitting damage.

4.4. Probabilistic Imaging

With *NIs* obtained from all sensing paths, the pitting damage location can be pinpointed, and the severity evaluated. To this end, the reconstruction algorithm for probabilistic inspection of damage (RAPID)[48] is recalled. In RAPID, the pitting damage is assessed in terms of the probability of its presence. In this way, the distribution probability of pitting damage is depicted in a contour map, yielding an intuitive and rapid diagnosis of the damage.

In this algorithm, the inspection region is spatially meshed, yielding a 2-D pixelated image on which the presence probability of damage at each spatial point is evaluated. Employing a sensing path $P_n(n=1,2,3,\cdots)$ with transducer and receiver at (x_i, y_i) and (x_j, y_j), respectively, the field value at pixel (x, y) obtained via this sensing path is depicted as

$$\xi(x,y)_n = NI_n[\frac{\eta - R_n(x,y)}{\eta - 1}], \tag{7}$$

where *NI* is the defined damage index in the designated path, η is the scaling parameter controlling the size of the elliptical influence region of individual sensing paths, and its value is usually set to be 1.05. $D_n(x,y)$ is a parameter reflecting the distance from the pixel to the sensing path, $R_n(x,y)$ is a weight reflecting the influence of the sensing path on the pixel, which reads[7,48],

$$D_n(x,y)=\frac{\sqrt{(x-x_i)^2+(y-y_i)^2}+\sqrt{(x-x_j)^2+(y-y_j)^2}}{\sqrt{(x_i-x_j)^2+(y_i-y_j)^2}},$$
$$R_n(x,y)=\begin{cases} D_n(x,y) & \text{when} \quad D_n(x,y)<\eta, \\ \eta & \text{when} \quad D_n(x,y)\ \geq\ \eta. \end{cases} \qquad (8)$$

With Eq. (7), each individual sensing path P_n yields a predictive image, describing the presence probability and severity of pitting damage at each pixel, and the pixels in the damaged inspection region show a fairly high field value while a low field value is ascertained at pixels in the intact inspection region. With the field values, various elliptical loci with focus on the two pixels corresponding to the actuator and sensor are ascertained. The field value gradually decreases with the distance of the concerned pixel to the two foci.

Considering that the pitting damage is distributed over a wide region and each sensing path is only sensitive to pixels close to it, an image fusion scheme is exploited to synthesize imaging results from all sensing paths. In this way, an ultimate image is constructed, which collects all the prediction from this network. As an extra merit, the measuring noise and the detection uncertainty introduced in the scanning procedure can be significantly suppressed due to the synthesis processing. The image fusion scheme is defined as

$$\xi(y,z)_{sum}=\frac{1}{M}\sum_{j=1}^{n}\xi(y,z)_j, \qquad (9)$$

where $\xi(x,y)_{sum}$ is the field value at pixel (x,y) in the ultimate superposed image. $M=\sum_n He(\eta-R_n(x,y))$ is the count for the pixel (x,y) in the inspection region of a path.

The imaging results of pitting damage incurred by both normal and oblique HVI, using RAPID, are shown in Figure 17. The pixels with high field values are displayed in the central region (*i.e.*, the orange area) of pitting damage, and relatively lower field values are observed for some pixels adjacent to the region of pitting damage, giving users an intuitive and quantitative perception about the pitting damage. With a threshold field value, the HVI-induced pitted region is highlighted in the inspection region, the occurrence and severity of pitting damage are revealed more clearly in Figure 18. It is noteworthy that a circular pitted region with various damage levels (corresponding to D_{cc}, D_{rc} and D_{99}) is formed under normal HVI, as exhibited in Figure 18(a). Two separated pitted regions (*i.e.*, the yellow regions) with the highest pixel values corresponds to oblique HVI-induced A_{d1} and A_{d2}, as displayed in Figure 18(b). The location and size of the reconstructed pitted regions are consistent with the real pitting damage areas induced by normal and oblique HVI.

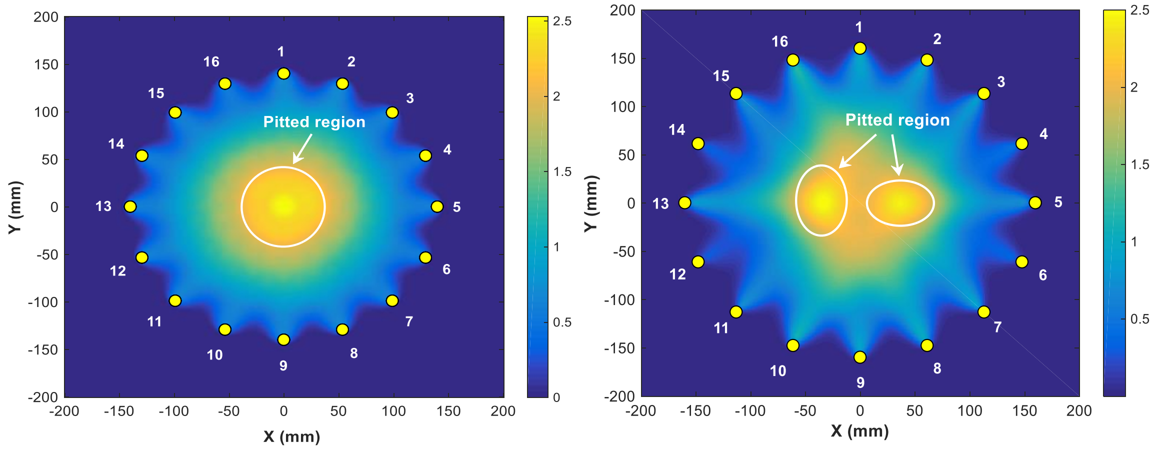

(a) (b)

Figure 17. Diagnostic images obtained by RAPID: (a) normal HVI scenario; and (b) oblique HVI scenario.

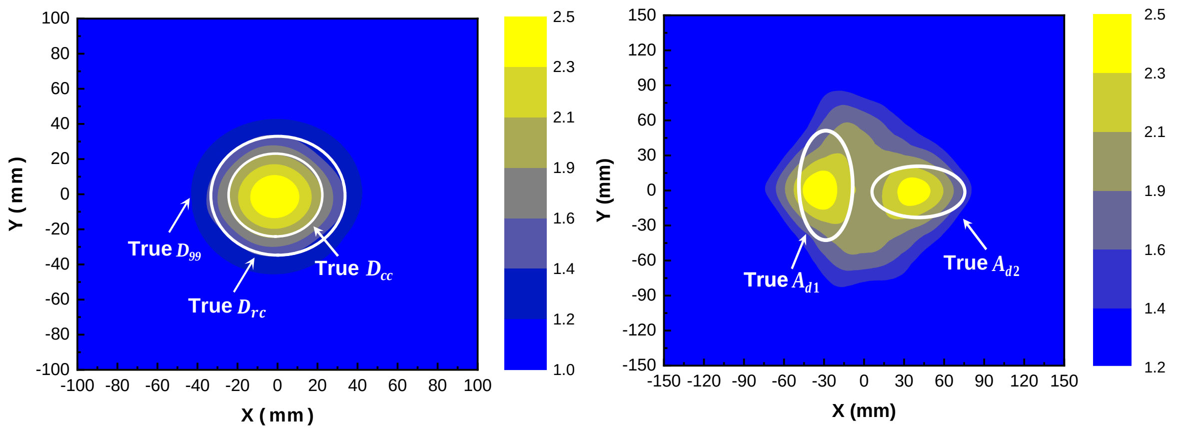

(a) (b)

Figure 18. Diagnostic images obtained by RAPID with a threshold value: (a) normal HVI scenario; and (b) oblique HVI scenario.

5. Conclusion

Featuring hundreds of localized craters, cracks and diverse microscopic defects disorderedly clustered over a wide region, the pitting damage induces highly complex wave scattering in a linear regime. Targeting characterization of the pitting damage in a holistic manner (mainly the presence, location and size of the pitted area), an insight into the generation of nonlinear features (*i.e.*, second harmonic mode) in probing GUWs that are induced by pitting damage is achieved via theoretical and a SAFE method. In the pitted region, material nonlinearity is significantly enhanced, and the CAN is introduced by the interaction between the probing GUWs and the pitting damage, both jointly contributing to the intensification of nonlinear features in the GUWs. On this basis, an *NI* is proposed to link the degree of nonlinearity to the size of pitting damage, which manifests a significant enhancement in GUWs traversing the pitted region. With the *NI*, a SHM framework, utilizing an *in-situ* PZT network, is established, and in conjunction with the use of the RAPID algorithm, to visualize pitting damage and monitor material deterioration progress continuously. The proposed framework is experimentally validated by precisely characterizing highly complex pitting damage of different modalities in a space structure, engendered by a hypervelocity debris cloud. Essentially all these *NIs* are obtained as the current status, without entailing a benchmark process against baseline signals from an intact counterpart, and thus this proposed approach offers a baseline-free mechanism to characterize pitting damage.

Acknowledgements

This project was funded by the National Natural Science Foundation of China (Nos. 51875492, 11772113 and 51635008) and the Hong Kong Research Grants Council via General Research Fund (Nos. 15201416, 15212417 and 15204419).

References

[1] Jakubowski M. Influence of pitting corrosion on fatigue and corrosion fatigue of ship and offshore structures, part II: load-PIT-crack interaction. *Pol Marit Res* 2015; 22: 57-66.

[2] Bhandari J, Khan F, Abbassi R, et al. Modelling of pitting corrosion in marine and offshore steel structures-A technical review. *J Loss Prevent Proc* 2015; 37: 39-62.

[3] Metallurgical Consulting. http://www.metalconsult.com/stress-corrosion-cracking-reactor-vessel.html (accessed 09 August 2019).

[4] Chatterton S, Pennacchi P and Vania A. Electrical pitting of tilting-pad thrust bearings: Modelling and experimental evidence. *Tribol Int* 2016; 103: 475-486.

[5] Raadnui S and Kleesuwan S. Electrical pitting wear debris analysis of grease-lubricated rolling element bearings. *Wear* 2011; 271: 1707-1718.

[6] Cao W, Wang Y, Zhou P, et al. Microstructural material characterization of hypervelocity-impact-induced Pitting Damage. *Int J Mech Sci* 2019; 163:105097.

[7] Liu M, Wang K, Lissenden C J, et al. Characterizing hypervelocity impact (HVI)-induced pitting damage using active guided ultrasonic waves: from linear to nonlinear. *Materials* 2017; 10: 547.

[8] Guan G, Pang B, Zhang W, et al. Crater distribution in the rear wall of AL-Whipple shield by hypervelocity impacts of AL-spheres. *Int J Impact Eng* 2008; 35(12), 1541-1546.

[9] Murr L, Quinones S A, Ayala A, et al. The low-velocity-to-hypervelocity penetration transition for impact craters in metal targets. *Mat Sci Eng A-Struct* 1998; 256: 166-182.

[10] Moser D, Poelchau M H, Stark F, et al. Application of nondestructive testing methods to study the damage zone underneath impact craters of MEMIN laboratory experiments. *Meteorit Planet Sci* 2013; 48: 87-98.

[11] Raith M and Grosse C U. In ultrasound tomography on hypervelocity impact targets. *In 19th World Conference on Non-Destructive Testing*, Deutsche Gesellschaft f€ ur Zerst€ orungsfreie Pr€ ufung DGZfP, Th, 2016; 2016; p A4.

[12] Su Z, Ye L. Lamb wave propagation-based damage identification for quasi-isotropic CF/EP composite laminates using artificial neural algorithm: Part II - Implementation and Validation. *J Intel Mat Syst Str* 2005; 16(2): 113-125.

[13] Cao W, Zhou P, Liao Y, et al. A spray-on, nanocomposite-based sensor network for *in-situ* active structural health monitoring. *Sensors* 2019; 19(9): 2077.

[14] Wang K, Liu M, Cao W, et al. Detection and sizing of disbond in multilayer bonded structure using modally selective guided wave. *Struct Health Monit* 2019: 1475921719866274

[15] Lu Y and Michaels J E. A methodology for structural health monitoring with diffuse ultrasonic waves in the presence of temperature variations. *Ultrasonics* 2005; 43: 717-731.

[16] Ong W H and Chiu W K. Enhancement of Lamb wave-based in situ structural health monitoring through guided local geometry changes. *Struct Health Monit* 2013; 12: 339-358.

[17] Zhou P, Liao Y, Li Y, et al. An inkjet-printed, flexible, ultra-broadband nanocomposite film sensor for in-situ acquisition of high-frequency dynamic strains. *Compos Part A-Appl S* 2019; 125: 105554.

[18] Jhang K-Y. Nonlinear ultrasonic techniques for nondestructive assessment of micro damage in material: a review. *Int J Precis Eng Manuf* 2009; 10: 123-135.

[19] Felice M V, Fan Z. Sizing of flaws using ultrasonic bulk wave testing: A review. *Ultrasonics* 2018; 88: 26-42.

[20] Dutta D, Sohn H, Harries K A, et al. A nonlinear acoustic technique for crack detection

in metallic structures. *Struct Health Monit* 2009; 8: 251-262.

[21] Solodov I, Wackerl J, Pfleiderer K, et al. Nonlinear self-modulation and subharmonic acoustic spectroscopyfor damage detection and location. *Appl Phys Lett* 2004; 84: 5386-5388.

[22] Ulrich T, Johnson P A and Müller M, et al. Application of nonlinear dynamics to monitoring progressive fatigue damage in human cortical bone. *Appl Phys Lett* 2007; 91: 213901.

[23] Wang X, Wang X, Hu X, et al. Damage assessment in structural steel subjected to tensile load using nonlinear and linear ultrasonic techniques. *Appl Acoust* 2019; 144, 40-50.

[24] Setyawan W, Henager Jr C H and Hu S. Nonlinear ultrasonic response of voids and Cu precipitates in body-centered cubic Fe. *J Appl Phys* 2018; 124(3), 035104.

[25] Cantrell J H. Substructural organization, dislocation plasticity and harmonic generation in cyclically stressed wavy slip metals. *Proceedings of the Royal Society of London. Series A: Mathematical, Physical and Engineering Sciences* 2004; 460(2043), 757-780.

[26] Pruell C, Kim J-Y, Qu J, et al. Evaluation of fatigue damage using nonlinear guided waves. *Smart Mater Struct* 2009; 18: 035003.

[27] Meo M, Polimeno U and Zumpano G. Detecting damage in composite material using nonlinear elastic wave spectroscopy methods. *Appl Compos Mater* 2008; 15: 115-126.

[28] Li F, Meng G, Kageyama K, et al. Optimal mother wavelet selection for lamb wave analyses. *J Intel Mat Syst Str* 2009; 20(10): 1147-1161.

[29] Wang K, Cao W, Liu M, et al. Advancing Elastic Wave Imaging Using Thermal Susceptibility of Acoustic Nonlinearity. *Int J Mech Sci* 2020: 105509.

[30] Semperlotti F, Wang K and Smith E C. Localization of a breathing crack using super-harmonic signals due to system nonlinearity. *AIAA journal* 2009; 47(9): 2076-2086.

[31] Solodov I Y, Krohn N and Busse G. CAN: an example of nonclassical acoustic

nonlinearity in solids. *Ultrasonics* 2002; 40: 621-625.

[32] Wang K, Liu M, Su Z, et al. Analytical insight into “breathing” crack-induced acoustic nonlinearity with an application to quantitative evaluation of contact cracks. *Ultrasonics* 2018; 88: 157-167.

[33] Wang K, Li Y, Su Z, et al. Nonlinear Aspects of “Breathing” Crack-disturbed Plate Waves: 3-D Analytical Modeling with Experimental Validation. *Int J Mech Sci* 2019; 159: 140-150.

[34] Biwa S, Nakajima S and Ohno N. On the Acoustic Nonlinearity of Solid-Solid Contact With Pressure-Dependent Interface Stiffness. *Appl Mech-T Asme* 2004; 71: 508-515.

[35] Xiang Y, Zhu W, Deng M, et al. Experimental and numerical studies of nonlinear ultrasonic responses on plastic deformation in weld joints. *Chinese Phys B* 2015; 25(2), 024303.

[36] Xiang Y, Deng M, Liu C, et al. Contribution of mixed dislocations to the acoustic nonlinearity in plastically deformed materials. *J Appl Phys* 2015; 117: 214903.

[37] Davoudi K M and Vlassak J J. Dislocation Evolution During Plastic Deformation: Equations vs. Discrete Dislocation Simulations. *arXiv preprint arXiv* 2014; 1408.6609.

[38] de Lima W and Hamilton M. Finite-amplitude waves in isotropic elastic plates. *J Sound Vib* 2003; 265: 819-839.

[39] Landau L D, Lifshitz E M, Sykes J B, et al. Theory of elasticity: Vol. 7 of course of theoretical physics. *Phys Today* 1960; 13: 44.

[40] Kumar A, Torbet C J, Jones J W, et al. Nonlinear ultrasonics for in situ damage detection during high frequency fatigue. *J Appl Phys* 2009; 106(2): 024904.

[41] Stobbe D M. *Acoustoelasticity in 7075-T651 Aluminum and Dependence of Third Order Elastic Constants on Fatigue Damage*. Georgia, United Stated, Georgia Institute of Technology, 2005.

[42] Yost W T and Cantrell J H. Materials characterization using acoustic nonlinearity parameters and harmonic generation: engineering materials. In *Review of Progress in Quantitative Nondestructive Evaluation*. Springer, Boston, MA, 1990: 1669-1676.

[43] Zhu W, Xiang Y, Liu C, et al. Fatigue damage evaluation using nonlinear Lamb Waves with Quasi phase-velocity matching at low frequency. *Materials* 2018; 11(10): 1920.

[44] NACE International. https://www.nace.org/resources/general-resources/corrosion-basics/group-2/intergranular-corrosion (accessed 09 June 2019).

[45] Metallurgical Technologies, Inc., P.A. https://www.met-tech.com/metallography/ (accessed 09 June 2019).

[46] Matsuda N and Biwa S. Phase and group velocity matching for cumulative harmonic generation in Lamb waves. *J Appl Phys* 2011; 109(9): 094903.

[47] Deng M and Xiang Y. Analysis of second-harmonic generation by primary ultrasonic guided wave propagation in a piezoelectric plate. *Ultrasonics* 2015; 61, 121-125.

[48] Zhao X, Gao H, Zhang G, et al. Active health monitoring of an aircraft wing with embedded piezoelectric sensor/actuator network: I. Defect detection, localization and growth monitoring. *Smart Mater Struct* 2007; 16: 1208.